

Testing of the analytical anisotropic algorithm for photon dose calculation

Ann Van Esch^{a)}

7Sigma, QA-team in Radiotherapy Physics, Belgium and Clinique Ste Elisabeth, Namur, Belgium

Laura Tillikainen

Varian Medical Systems, Helsinki, Finland

Jukka Pyykkonen and Mikko Tenhunen

Helsinki University Hospital, Helsinki, Finland

Hannu Helminen, Sami Siljamäki, and Jyrki Alakuijala

Varian Medical Systems, Helsinki, Finland

Marta Paiusco and Mauro Iori

San Maria Nuova Hospital, Reggio Emilia, Italy

Dominique P. Huyskens

7Sigma, QA-team in Radiotherapy Physics, Belgium and Clinique Ste Elisabeth, Namur, Belgium

(Received 13 March 2006; revised 9 May 2006; accepted for publication 9 June 2006; published 17 October 2006)

The analytical anisotropic algorithm (AAA) was implemented in the Eclipse (Varian Medical Systems) treatment planning system to replace the single pencil beam (SPB) algorithm for the calculation of dose distributions for photon beams. AAA was developed to improve the dose calculation accuracy, especially in heterogeneous media. The total dose deposition is calculated as the superposition of the dose deposited by two photon sources (primary and secondary) and by an electron contamination source. The photon dose is calculated as a three-dimensional convolution of Monte-Carlo precalculated scatter kernels, scaled according to the electron density matrix. For the configuration of AAA, an optimization algorithm determines the parameters characterizing the multiple source model by optimizing the agreement between the calculated and measured depth dose curves and profiles for the basic beam data. We have combined the acceptance tests obtained in three different departments for 6, 15, and 18 MV photon beams. The accuracy of AAA was tested for different field sizes (symmetric and asymmetric) for open fields, wedged fields, and static and dynamic multileaf collimation fields. Depth dose behavior at different source-to-phantom distances was investigated. Measurements were performed on homogeneous, water equivalent phantoms, on simple phantoms containing cork inhomogeneities, and on the thorax of an anthropomorphic phantom. Comparisons were made among measurements, AAA, and SPB calculations. The optimization procedure for the configuration of the algorithm was successful in reproducing the basic beam data with an overall accuracy of 3%, 1 mm in the build-up region, and 1%, 1 mm elsewhere. Testing of the algorithm in more clinical setups showed comparable results for depth dose curves, profiles, and monitor units of symmetric open and wedged beams below d_{\max} . The electron contamination model was found to be suboptimal to model the dose around d_{\max} , especially for physical wedges at smaller source to phantom distances. For the asymmetric field verification, absolute dose difference of up to 4% were observed for the most extreme asymmetries. Compared to the SPB, the penumbra modeling is considerably improved (1%, 1 mm). At the interface between solid water and cork, profiles show a better agreement with AAA. Depth dose curves in the cork are substantially better with AAA than with SPB. Improvements are more pronounced for 18 MV than for 6 MV. Point dose measurements in the thoracic phantom are mostly within 5%. In general, we can conclude that, compared to SPB, AAA improves the accuracy of dose calculations. Particular progress was made with respect to the penumbra and low dose regions. In heterogeneous materials, improvements are substantial and more pronounced for high (18 MV) than for low (6 MV) energies. © 2006 American Association of Physicists in Medicine. [DOI: 10.1118/1.2358333]

I. INTRODUCTION

Accuracy in treatment planning systems (TPSs) has always been a concern in modern radiotherapy. In terms of quality control of treatment planning systems, different approaches have been used to investigate the accuracy of newly developed algorithms; for the testing of the algorithms in homogeneous conditions, several authors have compared calculated

dose distributions against their own measurements,¹⁻¹¹ against the test package provided by the AAPM¹² or against Monte-Carlo calculations;¹³ for the testing of algorithms in heterogeneous conditions, most work has focused on the testing of the lung.^{9-11,13-17}

Over the last years, a conviction has grown that precise dose calculation will necessitate the use of Monte-Carlo

methods to take correctly into account the electron transport governing the dose deposition process. However, Monte-Carlo methods are presently still too time consuming to be used in routine environments. Hence, any improvement in the existing algorithms is considered as valuable. Treatment planning algorithms for photon dose distributions have changed from two-dimensional (2D) algorithms to three-dimensional (3D) algorithms with a variety of subtle differences between 2D and 3D (the so-called 2.5D). In terms of the core part of the developed calculation engines, two fundamentally different approaches have been used over the last decades and implemented in commercial TPSs:

- Clarkson-Cunningham integration methods: in this approach the beam is divided in a primary component and a scatter component. The scatter component is calculated from a scatter function derived from experimental tissue phantom ratios. This type of calculation methods have been successfully implemented in commercial TPSs [e.g., Isis, Dosigray, Isogray (Dosisoft, France) and various other commercial systems].
- Scatter kernel dose calculations: in this approach the dose is calculated as a superposition of scatter contributions generated by kernels interacting with the tissue. In the simplest formalism, the scatter kernels are single pencil beams; ideally the scatter kernels should be 3D point spread functions representing the interaction of the photon beam in each voxel. Scatter kernel calculations have been successfully implemented in different commercial systems: e.g., pencil beam calculation methods were implemented in Plato (Nucletron, Netherlands) or in Cadplan (Varian Medical Systems, US); a more sophisticated technique, a development towards the point kernels, has been the collapsed cone convolution model.¹⁸ The collapsed cone convolution model was implemented in the Helax TPS (Nucletron, The Netherlands) and in the Pinnacle TPS (Philips, United Kingdom).

The dose calculation algorithm implemented into the Eclipse (Varian Medical Systems, US) treatment planning system is referred to as AAA (analytical anisotropic algorithm). The implementation of AAA was split up into a configuration part and a dose calculation part. For the configuration part, an optimization method was developed to determine the parameters for a multiple source model by means of the basic beam data measurements and the dose calculation algorithm. Should the AAA dose calculation algorithm be replaced by a more sophisticated one, the configuration engine can be used for this new algorithm as well. With respect to the dose calculation part, AAA is based on the algorithm originally developed by Ulmer *et al.*^{19–22} Compared to the work by Ulmer *et al.*, exponential functions are now used instead of Gaussian functions to better model the scatter near borders of lateral heterogeneities. Furthermore, some simplifications were made in the modeling of the dose in the build-up region to significantly reduce the time required for dose calculation. AAA was developed to replace the single pencil beam (SPB)

model developed by Storchi *et al.*²³ The inhomogeneity correction, especially in the lung, was known to be suboptimal with the SPB; AAA should provide a better modeling of the dose deposition in the lung and at the interfaces of lung-tumor or lung-tissue.

A first characterization of the AAA algorithm in water was published by Fogliata *et al.*²⁴ in their investigation of the configuration module of the AAA algorithm, they reported an accuracy of 1% to 2% for output factors of open and wedged beams, respectively, a 1%, 1 mm average accuracy in the calculated depth dose curves and an accuracy within 1% for the central region of the profiles. As a whole, they concluded that their basic beam data were satisfactorily reproduced by the AAA configuration module.

Because users are allowed a substantial amount of freedom in the acquisition of the basic beam data and the calibration of the treatment units (source-phantom distance, depth of calibration, depth of measurement, etc.), and because the beam configuration is expected to depend considerably on the quality of the beam data, we report on the testing of the AAA configuration in three different radiotherapy departments. One of the goals of this article is to provide some starting data (calculated profiles, depth dose curves, etc.) about the accuracy that should be obtained when configuring AAA in the Eclipse treatment planning system. We have also aimed at describing the AAA dose calculation model, the specific improvements and limitations, and their effects on the accuracy of the dose calculation. Regarding the acceptance of the dose calculation module, we have performed a series of measurement setups in simple as well as in extreme conditions, in water as well as in heterogeneous material.

II. DESCRIPTION OF THE AAA ALGORITHM

The AAA algorithm was developed by the research group of Varian Medical Systems in continuation of the work by Ulmer *et al.*^{19–22} An extensive description will be published separately by these authors themselves. However, for completeness, an overview of the algorithm is presented below.

The implementation of the analytical anisotropic algorithm for the calculation of dose distribution for photon beams consists of two parts: the configuration module and the dose calculation module.

A. The configuration module

The purpose of this module is to characterize the phase space of a photon beam of a linear accelerator. The phase space (particle, fluence, energy) is approximated using a multiple source model:²⁵ a point source for radiation from the target, a finite source for extra focal radiation, and a third source to model the electron contamination.

In the configuration module, each source is modeled by optimizing a number of parameters and correction curves in order to obtain the best agreement between calculated and measured basic beam data. The basic beam data are not re-measured for AAA, but are the ones acquired for the SPB configuration. A complete description of the mathematical

optimization methods used for determining the physical parameters of the multiple source model is beyond the scope of this paper and will be published separately. In summary, the beam configuration engine first processes the measured beam data and checks for possible measurement inaccuracies (e.g., small offsets in the zero position in profiles, missing side scatter for large-field half-profiles because of limited dimensions of water phantoms, etc.). If possible, these inaccuracies are corrected for, if not, a warning is issued and the involved data are excluded from the optimization process. During optimization, the source model is used as an input for the dose calculation by means of the AAA algorithm (described in subsection II B) in a homogeneous water phantom. The cost function to be optimized includes the difference between beam data measurements and AAA dose calculation as well as a penalty term to penalize unphysical parameter values. As an illustration, some of the beam characterizing parameters and curves as produced by the configuration process are shown for a 6 and an 18 MV beam in Fig. 1.

1. The primary photon source

The initial photon spectra resulting from bremsstrahlung interaction of the electron beam impinging on the target were precalculated using Monte-Carlo methods.^{26,27} This was done for the different existing targets in the Varian accelerators [Fig. 1(a)]. To take into account the beam hardening effect of the flattening filter, a mean energy radial curve is introduced, i.e., the mean energy of the photon beam decreases with increasing distance from the central axis [Fig. 1(b)]. Next, to take into account the variation of photon fluence below the flattening filter, a radial intensity profile is introduced [Fig. 1(c)]. The optimization of the mean energy radial curve and the radial intensity profile should mainly generate correct depth dose curves below the depth of maximum dose and accurate profiles between the beam axis and the penumbra region.

2. The extra-focal photon source (second source)

The extra focal photon source models the additional photons generated in the flattening filter, in the primary collimator, and the secondary jaws. It is modeled as a virtual source with a finite width located at the bottom plane of the flattening filter. Since the secondary source is closer to the isocenter than to the primary source, it produces a broader beam. Mathematically, the second source fluence is calculated as a convolution of the primary fluence and a Gaussian with a width proportional to the finite source, an approach similar to the one presented by Liu *et al.*²⁵ The model empirically derives the mean energy and relative intensity of the extra-focal photon spectrum (typical values are shown in Table I). The off-axis variation in the spectrum is not modeled. The finite size of the source, the mean energy, and the relative weight are important to adequately model the penumbra region of the beam.

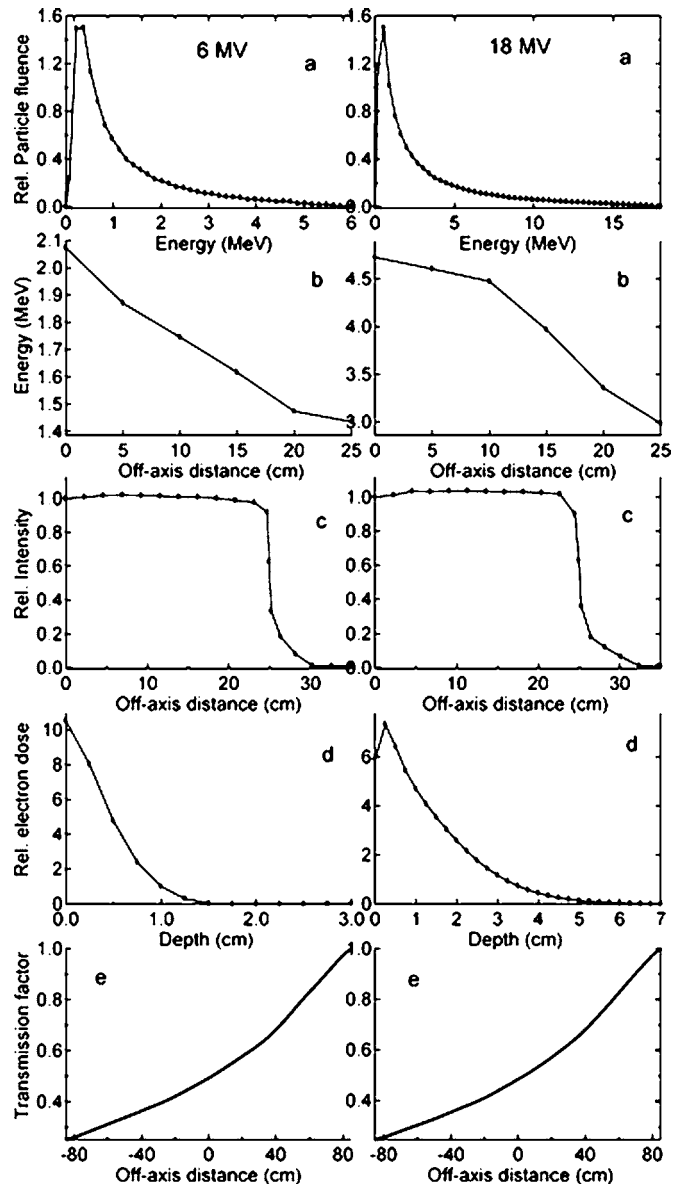


FIG. 1. Illustration of different curves produced during beam configuration for the characterization of the multiple source model for a 6 and an 18 MV photon beam: (a) unattenuated initial photon spectrum; (b) mean radial energy, modeling the beam hardening effect of the flattening filter; (c) radial intensity profile, modeling the variation of photon fluence below the flattening filter; (d) electron contamination, i.e., the total energy deposited by the contaminant electrons as a function of depth in water; and (e) wedge transmission curve (for the 60° physical wedge), i.e., the photon flux passing through a physical wedge without interaction. Data are in arbitrary units, unless indicated otherwise.

3. The electron contamination source

The electron contamination source models the electrons—created mainly by Compton interaction—in the head of the treatment unit and in air. The electron contamination source is viewed as a finite-size source located at the plane of the target. It is modeled by two Gaussians and one energy deposition function. The total energy deposited by the contaminant electrons as a function of depth in water is modeled by an empirical curve, determined from the difference between the measured depth dose and the depth dose calculated with

TABLE I. Typical values for second source and electron contamination parameters obtained for 6 and 18 MV beam data. The width of the Gaussians (σ_0 and σ_1) for the electron contamination is defined at the isocenter plane (SAD).

| | 6 MV | 18 MV |
|--|--------|--------|
| Second source parameters | | |
| Distance to primary source (mm) | 125 | 125 |
| Size (mm) | 39.3 | 36.6 |
| Relative intensity | 0.055 | 0.035 |
| Mean energy (MeV) | 1.0 | 1.0 |
| Electron contamination parameters | | |
| σ_0 (SAD) (mm) | 11.721 | 15.513 |
| σ_1 (SAD) (mm) | 66.008 | 72.089 |
| Relative fraction of σ_0 | 0.4108 | 0.3624 |

out contaminant electrons for the largest field size [Fig. 1(d) shows an illustration of such curves]. The effect of the energy spectrum is included implicitly in this empirical curve. The Gaussian functions model the lateral spread caused by the finite size of the source and the spreading out of the electrons in water. The widths of the Gaussians σ_0 and σ_1 , as well as their relative weights c_0 and $1-c_0$, are determined at the isocenter plane during the optimization (typical values are shown in Table I). These parameters are optimized to model the field size dependence of the electron contamination dose. Accurate modeling of the electron contamination parameters should contribute to an improved dose calculation in the build-up region of the beam.

The above parameters are derived for open beams. Most beam modifying accessories are taken into account in the dose calculation through their impact on the primary photon fluence only. For blocks, the primary fluence is modified by means of the user-defined transmission factor. Parameters used to characterize the multileaf collimation (MLC) are the leaf transmission and the dosimetric leaf separation, the latter describing the rounded leaf tips; i.e., the effective dosimetric opening between mechanically closed leaf pairs. The effect of the beam modifying accessories on the second source and electron contamination source is modeled through their effect on the primary fluence before convolution with the Gaussians.

Physical wedges modify the photon fluence and the spectral characteristics of the beam. The photon flux passing through a physical wedge without interaction is modeled using a transmission curve [Fig. 1(e)], derived from the profile measurements along the wedge direction for the largest wedged field. The transmission curve determines how much the primary photon spectrum is hardened in the wedge and how much the fluence of the primary photons is attenuated. The second source parameters are copied from the open beam configuration, with the exception that the intensity of the second source is attenuated by the wedge transmission factor on the beam axis. AAA includes a dual-Gaussian source located at the wedge plane to model the photons that are scattered in the wedge. In the configuration process, the

intensity and energy of this additional scatter source are derived from a profile, measured perpendicular to the wedge direction. The widths of the Gaussians have been derived from Monte-Carlo simulations and are fixed. The electron contamination source is again only modeled through the changes in the primary fluence.

In the case of the enhanced dynamic wedge (EDW), movement of the Y-collimator generates a wedged profile. AAA uses the preconfigured STT tables (segment treatment data table) describing the movement of the Y main collimator for different wedge angles and the parameters for open beams as derived during the open beam configuration.

B. The dose calculation module

For volumetric dose distribution calculation, the clinical beam is divided into small beamlets and the patient body volume is divided into a matrix of 3D calculation voxels along these beamlets, the dimensions of which are determined by the selected calculation grid (minimum 2 mm). The geometry of the grid is divergent, aligning the coordinate system with the beam fanlines. Every calculation voxel is associated with a mean electron density that is computed from the patient CT images according to a user-defined calibration curve. The clinical beam is represented by two-dimensional fluence distributions describing the incident flux of photons and contamination electrons by means of the parameters derived during the configuration of the algorithm.

The final dose distribution is calculated as a superposition of the dose deposited by the primary and secondary photons and the contamination electrons for every beamlet.

1. Calculation of the dose deposited by the primary and the secondary source

The dose deposited by the primary and secondary photons is calculated in the same way, bearing in mind their different spectral composition and focal spot as determined during configuration of the beam parameters.

Using Monte-Carlo integration methods (EGSnrc^{26,27}), a set of monoenergetic kernels was constructed beforehand by calculating the pencil beam kernels $h_E(z, r)$ for narrow beams of monoenergetic photons of energy E , impinging on a semi-infinite water phantom; z is the distance from the surface, and r is the orthogonal distance from the central axis.

Although there is no separate heterogeneity correction step, the heterogeneity correction is performed only during the superposition phase. The first part of the calculation is performed as if the patient were a water equivalent medium.

Firstly, for every beamlet β , a polyenergetic pencil beam kernel $h_\beta(p)$ is constructed for every voxel p along the fanline by superposition of the above mentioned precalculated monoenergetic kernels, weighted by the spectrum of the beamlet. This polyenergetic pencil beam kernel is normalized to a single incident photon.

Secondly, the calculation model separates the energy deposition into depth directed (along the fanline) and lateral (perpendicular to the fanline) components.

The depth component $I_\beta(p_z)$ accounts for the total energy deposition of the pencil beam in the layer p_z :

$$I_\beta(p_z) = \Phi_\beta \iint h_\beta(x, y, p_z) dx dy. \quad (1)$$

The photon fluence Φ_β (i.e., the number of incident photons) is assumed to be uniform over the cross section of the beamlet β .

The lateral component $k_\beta(\theta, \lambda, p_z)$ is modeled as a sum of six radial exponential functions:

$$k_\beta(\theta, \lambda, p_z) = \sum_{i=1}^6 c_i \frac{1}{\mu_i} e^{-\mu_i \lambda}. \quad (2)$$

This component describes for each depth p_z and angle θ the fraction of energy deposited into an infinitesimally small angular sector at a distance λ to the central axis of the beamlet. The division of this lateral component into angular sectors is necessary for the heterogeneity correction as will be explained below. The attenuation coefficients μ_i are fixed for each plane and chosen such that the effective ranges $1/\mu_i$ vary between 1 and 200 mm. The weight parameters c_i are fitted to yield an optimal correspondence between the analytical kernel representation of Eq. (2) and the polyenergetic pencil beam constructed from the monoenergetic precalculated kernels.

In a homogeneous phantom, the energy deposited by a single beamlet β into an arbitrary point p in the plane p_z is the product of the total energy for this plane $I(p_z)$, multiplied by the scatter kernel:

$$E_\beta(p) = I_\beta(p_z) k_\beta(\theta, \lambda, p_z). \quad (3)$$

To account for heterogeneous patient tissue, it is assumed that each spatial dimension of the scatter process is scaled locally by the inverse relative electron density $1/\rho_w$:

$$\rho_w(p) \equiv \rho^{\text{el}}(p) / \rho_{\text{water}}^{\text{el}}. \quad (4)$$

In performing the heterogeneity correction, it is also assumed that the depth and lateral component can be independently scaled. This corresponds to pathways where particles are first assumed to arrive at the plane of destination via the central line of the beamlet and then scatter to the destination voxel in the lateral direction.

The depth-dependent component is scaled taking into account the radiological distance between the surface and the calculation points. Since this is an energy-based algorithm, it is also necessary to scale by local density. The depth-dependent component thus becomes

$$I'_\beta(p_z) = I_\beta(p'_z) \rho_w(p), \quad (5)$$

where p'_z is the effective depth.

For the scaling of the lateral scatter kernel, the water equivalent path length is calculated radially from the center of the beamlet. If λ' is the effective radius, the heterogeneity corrected lateral kernel is given by

$$k'_\beta(\theta, \lambda, p_z) = k_\beta\left(\theta, \frac{p'_z}{p_z} \lambda', p'_z\right) \rho_w(p). \quad (6)$$

It is also necessary to use the lateral scatter kernel from the effective depth p'_z , which is why the effective radius is also scaled by the ratio p'_z/p_z , correcting for the divergent coordinate system.

The final energy distribution in an arbitrary point p from a single beamlet β is then

$$E'_\beta(p) = I'_\beta(p_z) k'_\beta(\theta, \lambda, p_z). \quad (7)$$

In the computer implementation of the algorithm, a discrete number of 16 angular sectors was chosen and superposition is performed over these collapsed sectors. The total deposited energy in an arbitrary point p is then calculated as a summation of the contributions of all individual beamlets:

$$E_{\text{tot}} = \int \int_{\beta'} E'_\beta(p) d\beta'.$$

Finally, the energy distribution is converted to dose distribution by dividing by the local electron density.

2. Calculation of the dose deposited by contaminating electrons

Viewing the electron contamination as a finite-size source at the plane of the target, the fluence of the electron beam is modeled as a convolution of the primary fluence with a Gaussian (lateral spread σ_0). The dose deposited by the contaminating electrons is then calculated as the convolution of this electron fluence with a second Gaussian (lateral spread σ_1), multiplied with the electron energy deposition as a function of depth. As the latter is invariably used for all source to surface distances, changes in the electron spectrum with respect to the source to phantom distance used in the beam configuration are not accounted for.

3. Monitor unit (MU) calculation

The final formula for the MU calculation depends on the user-specific calibration geometry and the prescription method opted for by the user (dose per fraction, plan normalization, prescribed percentage, etc.). Apart from these factors, the MU calculation accounts for phantom scatter, head scatter, and collimator backscatter as follows. Both the phantom scatter factor and the head scatter factor (HSF) are derived through AAA dose calculation at the depth at which the output factors (OFs) were measured during configuration. The head scatter factors are only affected by the beam configuration parameters for the second source. The output factors are measured for different field sizes, allowing calculation of the collimator backscatter (CBSF) to the monitor chamber with the following formula:

$$\text{OF} = (\text{PSF} + \text{HSF}) \text{CBSF}.$$

The CBSF values are tabulated for a discrete number of rectangular field sizes (X, Y ranging from 3 to 40 cm) in the beam configuration.

III. OVERVIEW OF THE TESTING

A. Equipment and measurement methods

This work reports on the testing of the first clinically released AAA version (7.5.14.3) and the subsequent β -version (7.5.18.8). Acceptance was divided into testing of the beam configuration and the general dose calculation.

The AAA beam configuration requires the same basic beam input data as the SPB model: beam profiles and depth dose curves measured in a water phantom at five different depths for a number of square field sizes ranging from 3×3 to 40×40 cm². An output factor table for a series of rectangular field sizes (X and Y ranging from 3 to 40 cm) needs to be provided as well. Although a source-phantom distance (SPD) of 90 cm represents a more clinically relevant setup for isocentric treatments, for historical reasons, basic beam data measurements were performed at SPD = 100 cm for all participating centers. Profile measurements were acquired at depths d_{max} , 5, 10, 20, and 30 cm. The original configuration data (SPB) were measured with small diameter detectors: RK 0.12 cm³ (Wellhofer Scanditronix, Germany), IC15 0.13 cm³ (Wellhofer Scanditronix, Germany), PinPoint 0.015 cm³ (PTW, Germany), and a shielded p diode, type PFD^{3G} (Wellhofer Scanditronix, Germany). In two centers, output factors were obtained in isocentric conditions at 10 cm depth, SPD=90 cm. For one center, the output factor table was originally defined at depth of dose maximum and later remeasured at 10 cm depth. Before using them for AAA configuration, some of the profiles were cross-checked with a PTW diamond detector (TM60003, 0.0061 cm³). All centers used a NE 2571 thimble chamber for absolute point dose measurements.

For the acceptance testing of the dose calculation, most tests were performed at SPD=90 cm. All absolute dose measurements were corrected for daily fluctuations in the output of the accelerator by means of a cross-calibration in reference conditions. Furthermore, all relative dose measurements in a water phantom were converted to absolute dose by performing an absolute point dose measurement (on the beam axis for profiles, at 10 cm depth for depth dose curves) and by rescaling the measured curves to that point dose. Ion chamber measurements were performed with the same ion chambers as used for basic beam data acquisition. Planar measurements were performed with film (Kodak X-Omat Verification, US) or with the Seven29 2D ion chamber array (PTW, Germany). Gammex, RMI Solid Water plates (Cablon Medical, The Netherlands), and 2.5-mm-thick cork place-mats (IKEA, Sweden) were used for the construction of slab geometries. A 10-mm-thick cork slab from the same material was manufactured to hold the RK ion chamber. Calibration films to allow conversion from film density to dose were acquired during each film measurement session. Films were developed in a carefully monitored film developer (Agfa, Belgium) in the radiology department. The absolute level of the film dosimetry was cross-checked with an ion chamber measurement (single ion chamber or 2D ion chamber array) for every setup. The PTW Seven29 array is calibrated for absolute dosimetry. It consists of 27×27 ion chambers with

a square cross section of 5×5 mm² each and a center-to-center spacing of 10 mm between the chambers. For most measurement setups, two sets of data were acquired with the array shifted over 5 mm. The obtained images were merged, resulting in data with a 5 mm resolution.

Inhomogeneity tests were also performed in the intensity-modulated radiation therapy (IMRT) Thorax Phantom (Model 002LF, CIRS, Virginia, USA). This phantom has an elliptical shape and it represents an average human torso in density and in two-dimensional structures. According to the vendor, the tissue equivalent materials mimic the dosimetric properties (mass and electron density) of water, bone, and lung within 1%. The phantom contains rod inserts for either solid rods (for, e.g., the CT scan) or for ionization chamber measurements.

Although the grid in the AAA dose calculation can be set to 2 mm, all calculations in this work have been done with a calculation grid of 2.5 mm, corresponding to the internal resolution of the fluence.

B. Open field

Data on the dosimetric validation of the AAA configuration for open and wedged basic beam data (6 and 15 MV) in water have recently been published by Fogliata *et al.*²⁴ We have performed similar tests in three different centers, including 6 and 18 MV photon beams. Analysis of calculated versus measured depth dose curves and profiles (SPD = 100 cm) was performed qualitatively through visual comparison by means of overlays and quantitatively through a number of parameters. For profiles, the most critical part to model is the penumbra region. We have therefore used the distance to agree with the 80%, 50%, and 20% dose levels for quantitative analysis. For depth dose curves, we have used the dose difference at depths d_{max} , of 10 cm and 20 cm. In the calculation of monitor units, output factors are not used as such, but are split up into head scatter (without collimator backscatter), collimator backscatter, and phantom scatter. Hence, as a consistency check, monitor units were calculated in reference conditions for different field sizes to evaluate whether the original output factors could be reproduced.

Following the validation of the beam configuration, for the acceptance of the AAA dose calculation, profile and depth dose measurements were repeated in a water phantom with SPD=90 cm for a selection of square field sizes (6×6 , 10×10 , 15×15 , 20×20 , 25×25 cm²) for 6 and 18 MV. In addition, data were acquired for highly asymmetric fields by means of the 2D ion chamber array in solid water at a depth of 10 cm (SPD=90 cm). The mechanical limitations for creating asymmetric fields are determined by the maximum overtravel of the main collimators (-2 cm in the X direction, -10 cm in the Y direction). All fields were delivered and calculated for 100 MU. Because the 2D array measures absolute dose, these tests provide information on the profiles as well as on the MU calculation in highly asymmetric fields.

C. Wedged field

Similar to open beams, the accuracy of the modeling of physical wedged beams was first analyzed for the configuration beam data for the four existing wedge angles (15° , 30° , 45° , and 60°). As the enhanced dynamic wedge is based on the preconfigured tables describing the movement of the Y-collimator, it does not require any input data in the beam configuration other than the open beam data.

Secondly, for the validation of the algorithm in nonreference conditions, depth dose curves were measured for four field sizes (5×5 , 6×6 , 10×10 , and 15×15 cm²) for the 45° and 60° physical wedges at SPD=80, 90, and 100 cm to verify the accuracy of the modeling of the electron contamination as a function of source to skin distance. For both energies (6 and 18 MV), absolute profile measurements with the 2D ion chamber array at SPD=90 cm and at depths of 5, 10, and 20 cm, were performed for a series of square as well as asymmetric field sizes. All data were calculated and acquired for 200 MU.

For the verification of the EDW, absolute profiles were calculated on a phantom and compared to measurements with the 2D ion chamber array (for different wedge angles (15° , 30° , 45° , and 60°)). Measurements were performed at SPD=90 cm, at 5, 10, and 20 cm deep for multiple field sizes, symmetric (ranging from 5×5 to 20×20 cm²) as well as asymmetric ($X=20$ cm, $Y1=20$ cm, $Y2$ ranging from 20 to -10 cm) and two energies (6 and 18 MV). All EDW fields were delivered and calculated for 100 MU.

D. Static MLC shaped fields

We investigated the accuracy of calculated depth dose curves for MLC shaped fields as follows: with the main collimators set to 10×10 cm², depth dose curves were measured for square MLC shapes: 8×8 , 6×6 , and 4×4 cm². A C-shaped MLC plan was used as an extreme test case for the delivery of a narrow MLC field with the beam axis shielded. All tests were performed at SPD=90 cm.

E. IMRT fields

The sliding window solution of the Varian IMRT approach differs from the solution of other vendors primarily because the MLC is an additional field shaping device, not part of the main collimators: the IMRT fields are shaped by the movement of the MLC, while the main collimators retain an opening that is comparable to the field sizes used for conventional treatments. Hence, the small-field dosimetry problems are omitted and the MLC can be viewed as block replacement. Furthermore, the Eclipse inverse planning module does not make use of SPB or AAA but uses its own dose calculation algorithm to generate optimal fluences. These optimal fluences are converted into leaf motion files and their corresponding actual fluence by the leaf motion calculator. Hence, separate testing of the optimization process in the framework of the acceptance of AAA is not needed. However, adequate dose calculation based on the actual fluence remains crucial.

Dynamic MLC plans delivering dose by means of narrow sweeping gaps provide a critical test. In addition, it may occur that the fluence produced by the dynamic MLC encompasses only a small fraction of the total field opening (e.g., due to a very irregular shape of the target). Tests for these two extreme cases were combined by applying a sweeping gap of 1 cm for various square fluence dimensions (4×4 , 6×6 , 8×8 , 10×10 cm²) while keeping the main collimator opening at 10×10 cm². Depth dose curves were recorded with an ionization chamber in a water phantom (SPD=90 cm) for 6 and 18 MV. For every measurement point, the entire dynamic field had to be delivered. All calculations and measurements were performed with 200 MU. Additionally, a chair shaped test plan that has proved useful for IMRT validation with the SPB model²⁸ was calculated and measured at d_{\max} , 5, 10, 20, and 30 cm depth for 6 and 18 MV (SPD=90 cm). A detailed description of the chair test is given in Ref. 28. In summary, the shape of the chair is created such that the resulting dose delivery is very sensitive to the accuracy of the user-defined MLC parameters. Because of the narrow dimensions of the back and legs of the chair, modeling of the phantom scatter is also critical. Its regular shape facilitates analysis compared to clinical IMRT plans. Finally, a number of dynamic treatment fields were delivered to a homogeneous solid water phantom. Measurements of the chair and treatment fields were performed with the 2D ion chamber array. For the comparison of the measured and calculated 2D dose planes, we have used the gamma evaluation method^{29,30} as well as line profile overlays. Further testing of the IMRT modules was incorporated in the tests evaluating the inhomogeneity correction.

F. Inhomogeneity testing (cork, lung)

1. Profiles

As shown in Fig. 2(a), a 10-cm-thick cork slab inhomogeneity is incorporated into a solid water phantom. The total thickness of the phantom is 20 cm. The upper and lower part consist of 5 cm solid water plates; the middle contains partly solid water, partly cork. The beam axis is positioned in solid water at 2 cm from the cork in the lateral direction. This was done to avoid having the interface exactly along the beam axis and because in clinical setups, the isocenter is usually placed in the tumor, rather than in the lung tissue. Films are inserted in the phantom under 2 cm cork (d3), under 7 cm cork (d2), and in solid water at 0.5 cm below the solid water/cork slab (d1). Measurements were repeated with the 2D ion chamber array positioned directly below the solid water/cork slab: this corresponds to depth d1 since the effective measuring plane of the array is at 0.5 cm below the array surface. Data have been recorded for both 6 and 18 MV for the following field sizes $X \times Y$ [or $(X1+X2) \times Y$]: 6×6 , 8×8 , 10×10 , 15×15 , 20×20 , $(2+6) \times 8$, $(3+7) \times 10$, $(4+8) \times 12$ cm². The dimensions of the asymmetric fields were chosen to provide data that include equal amounts of cork and solid water in the irradiated area. All data were acquired with SPD=90 cm. For film measurements, dose delivery was restricted to 50 MU per field to avoid saturation of the film.

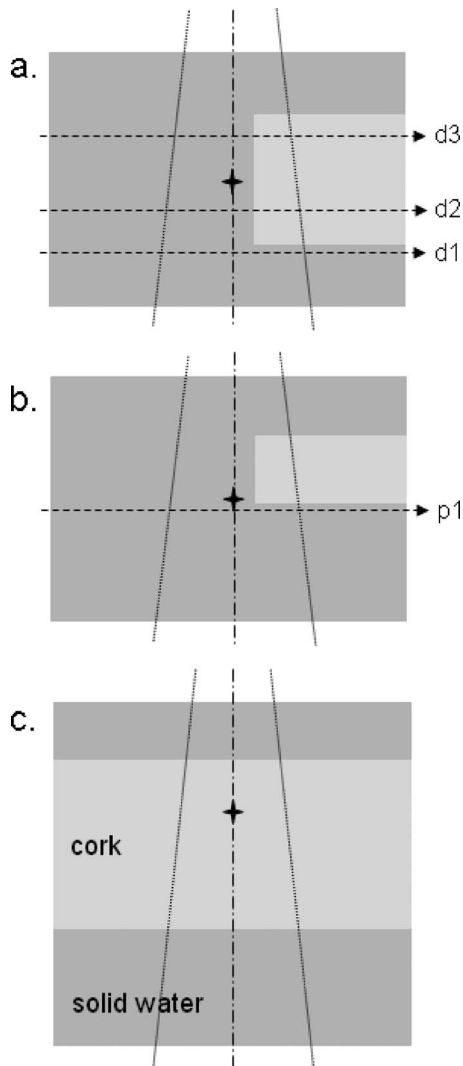


FIG. 2. (a) A 10-cm-thick cork/solid water inhomogeneity is sandwiched between two solid water plates 5 cm thick. The total thickness of the phantom is 20 cm. The beam axis is positioned at 2 cm from the cork in the lateral direction. Films (Kodak, EDR) are inserted in the phantom under 2 cm cork (d3), under 7 cm cork (d2), and at 0.5 cm below the cork/solid water slab (d1). The PTW ion chamber array is positioned under the cork (d1). (b) A 5-cm-thick cork/solid water inhomogeneity is sandwiched between solid water plates (5 cm thick and 10 cm thick). The beam axis is in solid water and positioned at 2 cm from the cork in the lateral direction. The PTW array is inserted right under the cork (p1). (c) A 15 cm cork slab is sandwiched between a 5 cm solid water slab and 10 cm solid water slab.

As shown in Fig. 2(b), a 5-cm-thick cork slab inhomogeneity is incorporated into a solid water phantom. The upper and lower homogeneous parts consist of solid water plates, 5 and 10 cm thick, respectively. The beam axis is in solid water and positioned at 2 cm from the cork in the isocenter plane (SPD=90 cm). The 2D ion chamber array is inserted immediately below the cork (p1), yielding an effective measuring plane at 0.5 cm from the cork. Data were recorded for 6 and for 18 MV and for the following field sizes: 6×6 , 8×8 , 10×10 , 12×12 , 15×15 , and 20×20 cm². To be consistent with the film data measurements, a delivery of 50 MU per field was used.

2. Depth dose curves

Depth dose curves were recorded in a phantom [Fig. 2(c)] consisting of solid water (5 cm), cork (15 cm), and solid water (10 cm). Discrete ionization chamber scans were recorded for 6 and 18 MV for various field sizes: 3×3 , 5×5 , 7×7 , 10×10 , 12×12 , 15×15 , and 20×20 cm² (SPD = 90 cm). All data were obtained for 100 MU.

3. Anthropomorphic measurements

A more clinical situation was simulated using the anthropomorphic phantom. To facilitate interpretation of the results, the phantom was irradiated with a single field (6 and 15 MV) set to 270°, as shown in Fig. 3. A dose of 2 Gy was calculated at the isocenter, placed in the middle of the phantom (i.e., in the mediastinum). Ionization chamber measurements were performed in the right and left lung and at the isocenter.

4. Inhomogeneity correction and IMRT

Combining IMRT and inhomogeneity testing, simple optimizations were performed on a range of thin rectangular patient target volumes (PTVs) created in the inhomogeneous phantom shown in Fig. 2(a): a homogeneous dose was requested in an inhomogeneous PTV. The width of the PTV was varied from 6 to 20 cm. (The length was kept fixed at 10 cm). After the dose volume optimizer had generated the corresponding optimal fluence, the forward calculation of the dose in the plane of the PTV was performed using AAA and SPB and measured with film.

IV. RESULTS

A. Open fields

Results on the open and wedged fields beam configuration data are very similar to the ones presented by Fogliata *et al.*²⁴ Therefore, only a limited selection of the analysis of the basic beam data is shown. Table II provides an illustration on the accuracy that was obtained in profile and depth dose calculation for different field sizes for 6 and 18 MV. Results in the different centers were very comparable. For each energy, the first part of the table gives the 80%, 50%, and 20% distance to agreement for field sizes ranging from 6×6 to 40×40 cm². The DTA is within 1 mm for the different field sizes in all centers. Secondly, the table illustrates the accuracy obtained for depth dose curves: the dose differences are within 1% for all field sizes at 10 and 20 cm depth, and within 2% at d_{max} . Thirdly, Table II shows that output factors calculated in reference conditions mostly agreed within 0.2% with the output factor table of the basic beam data.

Results on the testing of open fields in water in nonreference conditions are given in Table III and Figs. 4 and 5. Figure 4(a) shows an illustration of the measured and the calculated profiles for AAA and SPB (6 MV, 20×20 cm², four depths) for a source to phantom distance (SPD = 90 cm) that differs from the beam configuration setup. Considerable improvement around the penumbra region (i.e., inside the field, close to the field border, as well as outside

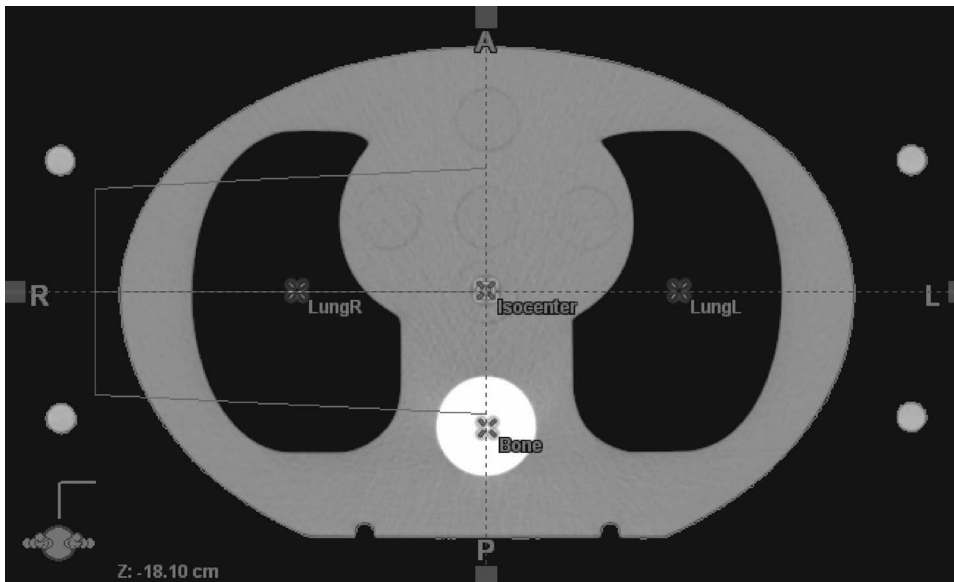


FIG. 3. Field setup of the irradiation of the anthropomorphic thorax phantom (Model 002LF, CIRS). Point dose measurements are performed in the center of the left and right lungs and in the mediastinum (isocenter).

the field) is observed for AAA compared to the SPB model. Although not displayed, results for other symmetrical field sizes and energies are very similar. Figure 4(b) shows the measured and calculated profiles of two half-beams in the X direction $[(X1+X2, Y)=(0+10, 20) \text{ cm}^2 \text{ and } (10+0, 20) \text{ cm}^2]$. Whereas the SPB overestimates the dose to the center of the half-beam field by $\sim 1.5\%$, AAA shows only a slight tendency to underestimate the dose ($\sim 0.5\%$). Figure 4(c) shows similar results for two half-beams in the Y direction $[(X, Y1+Y2)=(20, 0+10) \text{ cm}^2 \text{ and } (20, 10+0) \text{ cm}^2]$.

Figure 5 shows measured and calculated 18 MV depth dose curves for three field sizes (6×6 , 10×10 , and $20 \times 20 \text{ cm}^2$) at different SPD (90 and 100 cm). The SPB depth dose in reference conditions (SPD=100 cm) is only shown for the $20 \times 20 \text{ cm}^2$ field. As the SPB algorithm simply uses

the experimental curves as input in the algorithm, calculated and measured depth dose curves in reference conditions are by definition identical. Regarding AAA, even in reference conditions, small deviations (0.2 to 0.8%) are observed around d_{max} . Figure 5(a) shows that for SPD=90 cm, SPB and AAA have similar deviations around d_{max} ($\sim 0.5\%$), but SPB scores slightly better at depths shallower than d_{max} .

Table III shows the accuracy of the monitor unit calculation obtained for highly asymmetric field sizes (6 and 18 MV). Although the shape of the asymmetric profiles is well reproduced [e.g., Figs. 4(b) and 4(c)], AAA shows a tendency to underestimate the dose. The agreement is better for 18 MV than for 6 MV, where deviations of up to 3.1% are observed when both the X1 and Y1 collimator are moved to their mechanical limit for overtravel.

TABLE II. Overview of the obtained accuracy in the basic beam data reconstruction AAA (6 and 18 MV). Basic beam data were acquired at SPD=100 cm. Profile (Prof) data are listed at a depth of 5 cm, output factor (OF) are defined for SPD=90 cm at a depth of 10 cm. The 80%, 50%, and 20% distances to agreement reflect the quality of the penumbra modeling. The accuracy of the calculated depth dose is represented by the dose difference at depths d_{max} , 10 cm, and 20 cm.

| | | | $6 \times 6 \text{ cm}^2$ | $10 \times 10 \text{ cm}^2$ | $20 \times 20 \text{ cm}^2$ | $30 \times 30 \text{ cm}^2$ | $40 \times 40 \text{ cm}^2$ |
|-------|------|----------------------|---------------------------|-----------------------------|-----------------------------|-----------------------------|-----------------------------|
| 6 MV | Prof | DTA80 (mm) | 0.3/-0.2 | 0.7/-0.5 | 1.0/-0.6 | -0.8 | -1.5 |
| | | DTA50 (mm) | -0.3/0.5 | 0.0/0.5 | 0.7/0.4 | -0.3 | -0.9 |
| | | DTA20 (mm) | -1.0/1.0 | -0.6/1.0 | 0.3/0.4 | -0.3 | -1.8 |
| | DD | ΔD_{max} (%) | -1.6 | -1.7 | -1.4 | -1.0 | -0.8 |
| | | ΔD_{10} (%) | 0.3 | 0.2 | -0.6 | -0.1 | -0.3 |
| | | ΔD_{20} (%) | 0.4 | 0.3 | -0.3 | -0.3 | -0.6 |
| | OF | ΔD (%) | -0.2 | 0.0 | 0.0 | 0.1 | 0.2 |
| 18 MV | Prof | DTA80 (mm) | 0.1/0.1 | 0.1/-0.2 | 0.5/-1.0 | -0.7 | -0.2 |
| | | DTA50 (mm) | -0.2/0.2 | -0.2/0.1 | -0.1/-0.8 | -0.8 | -0.3 |
| | | DTA20 (mm) | -0.6/0.6 | -0.4/0.2 | -0.2/-0.4 | -0.9 | -0.3 |
| | DD | ΔD_{max} (%) | 0.2 | -0.7 | -0.8 | -0.9 | 0.0 |
| | | ΔD_{10} (%) | 0.2 | 0.0 | 0.4 | -0.3 | 0.0 |
| | | ΔD_{20} (%) | 0.2 | 0.1 | 0.2 | -0.4 | 0.1 |
| | OF | ΔD (%) | -0.1 | 0.0 | 0.0 | 0.2 | 0.3 |

TABLE III. Accuracy of the monitor unit calculation for highly asymmetric field dimensions. All fields were delivered and calculated for 100 MU, SPD=90 cm, depth=10 cm. Dose differences are given at the center of the fields.

| ΔD (AAA/IC)(%) | | Y1=0 cm Y2=20 cm | Y1=0 cm Y2=15 cm | Y1=0 cm Y2=10 cm | Y1=-5 cm Y2=20 cm | Y1=-10 cm Y2=20 cm |
|------------------------|----------------------|---------------------|---------------------|---------------------|----------------------|-----------------------|
| 6 MV | X1=0 cm X2=10 cm | -1.7 | -1.5 | -1.2 | -1.5 | -2.9 |
| | X1=0 cm X2=15 cm | -1.5 | -1.2 | -0.7 | -1.6 | -2.1 |
| | X1=0 cm X2=20 cm | -2.05 | -1.8 | -1.8 | -2.4 | -1.8 |
| | X1=-2 cm X2=20 cm | -2.5 | -2.1 | -2.0 | -2.8 | -3.1 |
| 18 MV | X1=0 cm X2=10 cm | 1.2 | 1.0 | 0.5 | -0.7 | -1.2 |
| | X1=0 cm X2=15 cm | -0.7 | -0.2 | -0.5 | -1.3 | -1.7 |
| | X1=0 cm X2=20 cm | -1.6 | -0.4 | -0.8 | -1.9 | -2.0 |
| | X1=-2 cm X2=20 cm | -2 | -1.2 | -1.1 | -1.5 | -1.9 |

B. Wedged fields

Results produced by the beam configuration optimization for physical wedges are comparable to those obtained for open fields, although deviations in the build-up area are increased to up to 3%, 1 mm. These findings are in agreement with already published data.²⁴

The accuracy of the modeling of wedges in non-reference field setups is represented by results shown in Fig. 6. The top part of the figure shows results for the physical wedge, whereas the bottom part displays data for the EDW. For both wedge types, measured versus calculated profiles are shown in the direction of the wedge and perpendicular to it. The displayed data are acquired with 6 MV for three field sizes (5×5 , $10 \times 10/12 \times 12$, and $15 \times 15/20 \times 20$ cm²) for a wedge angle of 60°. (For the 60° physical wedge, the field width is limited to 15 cm; for the EDW, it is limited to 20 cm). Although agreement between SPB and measurement improves for smaller field sizes, for clarity, the SPB calculation is only shown for the largest field sizes. Considerable improvement is noticed in the modeling of the slope of the wedge profile as well as in the beam profile perpendicular to the wedge direction when comparing AAA to SPB. Again, although somewhat less accurate than in open beams, the penumbra and the dose outside the field are more accurately calculated with AAA than with SPB. The absolute dose correspondence on the beam axis is within 0.5% for all symmetric field sizes.

Figure 7 displays wedged profiles of the 60° physical and enhanced dynamic wedge for 18 MV for a selection of asymmetric fields. For the physical wedge, the top part of the

figure shows wedged profiles for a 200 MU delivery of different field sizes ($X=15$ cm, $Y1=7.5$ cm, $Y2=7.5/5/0/-2.5/-5$ cm), and two profiles perpendicular to the wedge direction for half-beam wedged setups [($X1+X2, Y$)=(0

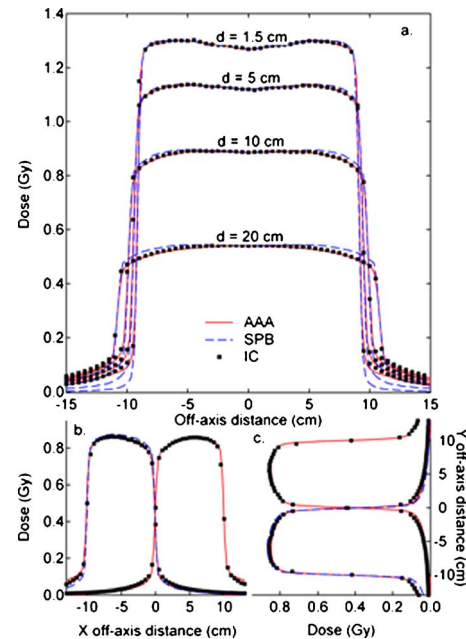


FIG. 4. Measured (IC) and calculated profiles for AAA and SPB for a 6 MV photon beam at SPD=90 cm for (a) a 20×20 cm² field at four different depths, (b) two half-beam profiles in the X direction at depth=10 cm, and (c) two half-beam profiles in the Y direction at depth=10 cm. All data correspond to a delivery of 100 MU.

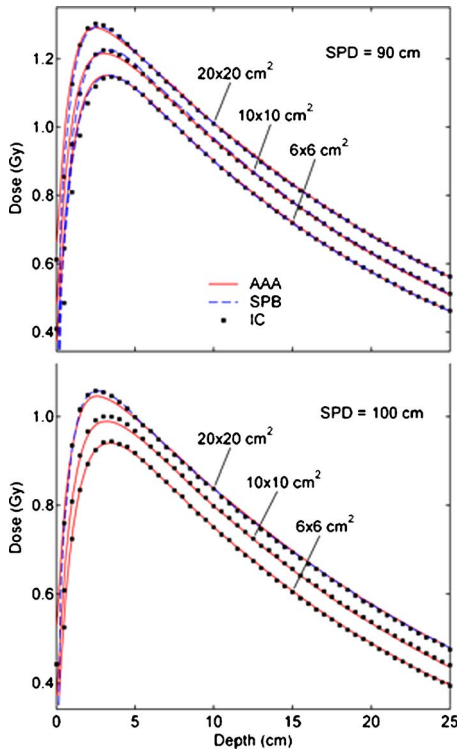


FIG. 5. Measured (IC) and calculated depth dose curves for 18 MV for three different field sizes (6×6 , 10×10 , and 20×20 cm²), at SPD=90 cm and SPD=100 cm. Absolute values correspond to a 100 MU delivery.

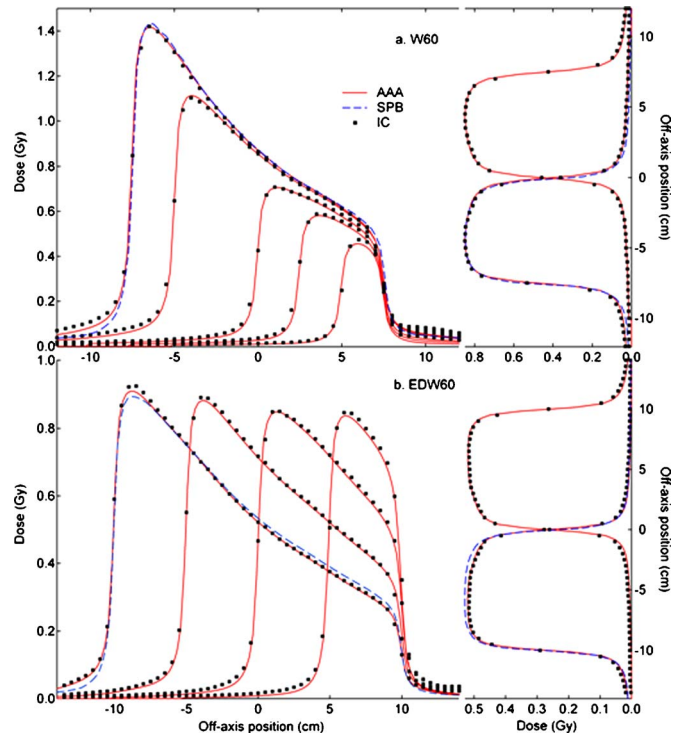


FIG. 7. Measured (IC) and calculated wedge profiles for AAA and SPB for asymmetric field sizes (18 MV, SPD=90 cm, depth=10 cm). On the left, profiles along the wedge direction are shown. On the right, profiles perpendicular to the wedge direction are shown. (a) Wedge profiles for a 60° physical wedge (W60) for different field sizes ($X=15$ cm, $Y_1=7.5$ cm, $Y_2=7.5/5/0/-2.5/-5$ cm), and two profiles perpendicular to the wedge direction for half beam wedged setups $[(X_1+X_2, Y)=(0+7.5, 15)$ and $(7.5+0, 15)$ cm²]. All W60 data are obtained with 200 MU. (b) Wedge profiles for a 60° enhanced dynamic wedge (EDW60) for different asymmetric field sizes ($X=20$ cm, $Y_1=10$ cm, $Y_2=10/5/0/-5$ cm) and two wedged half-beam profiles perpendicular to the wedge direction $[(X_1+X_2, Y)=(0+10, 20)$ and $(10+0, 20)$ cm²]. All EDW60 data are obtained with 100 MU. Field sizes are not shown in the graph but can be readily derived from the off-axis coordinates since all profiles are in the plane of the isocenter.

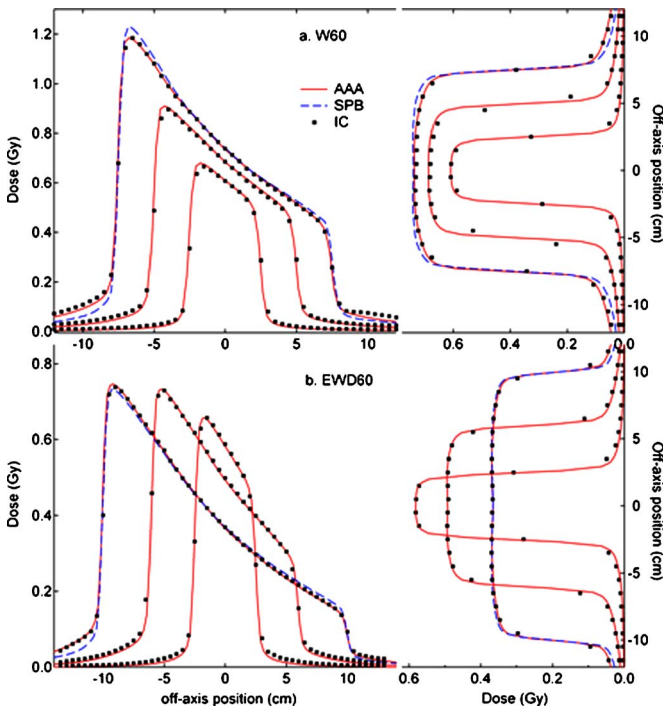


FIG. 6. Measured (IC) and calculated wedge profiles for AAA and SPB for symmetric field sizes (6 MV, SPD=90 cm, depth=10 cm). The graphs on the left show profiles along the wedge direction. The graphs on the right show profiles perpendicular to the wedge direction. (a) Wedge profiles for a 60° physical wedge (W60) for field sizes 5×5 , 10×10 , and 15×15 cm². All W60 data are obtained with 200 MU. (b) Wedge profiles for a 60° enhanced dynamic wedge (EDW60) for field sizes 5×5 cm², 12×12 cm² and 20×20 cm². All EDW60 data are obtained with 100 MU. For clarity, field sizes are not shown in the graph but can readily be derived from the off-axis coordinates since all profiles are in the plane of the isocenter.

+7.5, 15) and (7.5+0, 15) cm²]. Relative agreement of the profiles is excellent in both directions, but deviations up to 4% in the absolute dose at the center of the field are observed for the most pronounced asymmetries involving overtravel of the main collimator. The bottom part of Fig. 7 displays similar results for 100 MU deliveries with a 60° EDW for different asymmetric field sizes ($X=20$ cm, $Y_1=10$ cm, $Y_2=10/5/0/-5$ cm) and two wedged half-beam profiles perpendicular to the wedge direction $[(X_1+X_2, Y)=(0+10, 20)$ and $(10+0, 20)$ cm²]. AAA shows better correspondence with the measurement than SPB. The latter shows deviations up to 3% at the point of maximum dose and a somewhat inferior calculation of the slope of the wedged profile. Albeit smaller, deviations (up to 1.6%) at the point of maximum dose are also observed for AAA. Regarding the absolute dose in the center of the field, an overall difference of up to 1.5% is noticed for the most asymmetric fields ($Y_2=-5$ cm).

Figure 8 shows the depth dose behavior for a 15×15 cm² field with a 60° physical wedge, for 6 and 18 MV, for different source-to-phantom distances (SPD

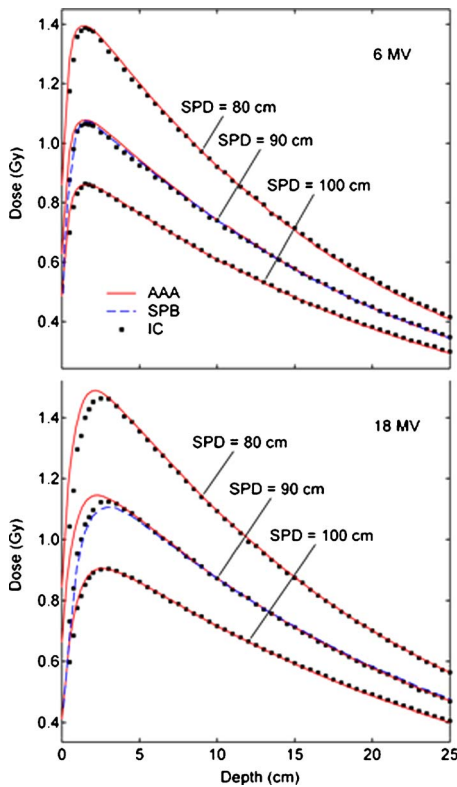


FIG. 8. Measured (IC) and calculated (AAA, SPB) depth dose curves for a $15 \times 15 \text{ cm}^2$ field with a 60° physical wedge, for 6 and 18 MV, for SPD = 80, 90, 100 cm. Absolute values correspond to a 200 MU delivery.

= 80, 90, 100 cm). For clarity, SPB data are again only displayed for SPD = 90 cm. For 6 MV, the measured and calculated (AAA and SPB) data agree within 1%, 1 mm, although the build-up behavior below d_{max} is slightly better modeled with SPB. For 18 MV, although the depth dose behavior in the beam configuration setup (SPD = 100 cm) is adequately reproduced by the calculation, discrepancies in the build-up area are substantial at smaller source-to-phantom distances.

C. Static MLC fields

Figure 9 illustrates measured and calculated absolute depth dose curves obtained for 8×8 , 6×6 , and $4 \times 4 \text{ cm}^2$ MLC fields with the main collimator set to $10 \times 10 \text{ cm}^2$ (100 MU, SPD = 90 cm, 18 MV). The two calculated depth dose curves correspond to the clinically released 7.5.14.3 version and to a corrected version of AAA (7.5.18.8) (only released for testing purposes). For version 7.5.14.3, overall divergence from the measured beam data increases as the MLC opening decreases. This observation was found to be related to a mistake in the calculation of the head scatter factor. As can be seen from Fig. 9, this has been corrected for in version 7.5.18.8.

Figure 10 shows two orthogonal beam profiles through the central axis of the C-shaped MLC delivery (100 MU, SPD = 95 cm, depth = 5 cm, 6 MV). In the Y direction, large discrepancies between calculation and measurement are found where opposing leafs close within the irradiated area (marked by the arrows in the figure). This discrepancy is

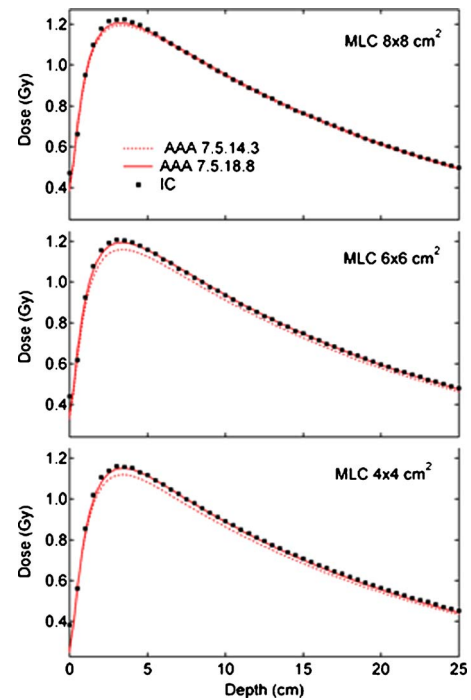


FIG. 9. Measured (IC) and calculated depth dose curves obtained for a 8×8 , 6×6 , and $4 \times 4 \text{ cm}^2$ static MLC field within a $10 \times 10 \text{ cm}^2$ field size. (SPD = 90 cm, 18 MV). The two calculated depth dose curves correspond to the clinically released 7.5.14.3 version and to a corrected version of AAA (7.5.18.8). Absolute values correspond to a 100 MU delivery.

related to the fact that the parameter modeling the rounded leaf ends (i.e., the dosimetric leaf separation) is not taken into account for static MLC fields. In the X direction, this is reflected in the slight underestimation of the absolute dose at the center of the MLC opening (0.7%) and in a small shift of the penumbra ($\sim 1 \text{ mm}$).

D. IMRT

Figure 11 illustrates depth dose curves obtained for a sweeping gap of 1 cm wide, generating square fluence patterns of 10×10 , 8×8 , 6×6 , and $4 \times 4 \text{ cm}^2$ in a fixed collimator opening of $10 \times 10 \text{ cm}^2$ (200 MU, SPD = 90 cm, 6 MV). AAA calculations are only shown for the corrected version (7.5.18.8). SPB and AAA model the depth dose behavior with a similar accuracy below d_{max} (1%, 1 mm). For the smallest fluence dimensions, AAA models the dose in the build-up area better than SPB. Even so, deviations of up to 2.5% are still observed at d_{max} .

A gamma evaluation comparing the calculation (AAA 7.5.18.8) and measurement for the dynamic chair delivery is shown in Fig. 12(a). Because of its inferior resolution, the (merged) 2D ion chamber measurement is always set as the reference in the calculation of the gamma index. For the chair, strict acceptance criteria of 2%, 2 mm were used. No line profiles for the chair delivery are shown since the obtained results are very similar to the ones published by Van Esch *et al.*²⁸ for the SPB. For the clinical IMRT field [Fig. 12(b)], criteria used for clinical routine IMRT verification (3%, 3 mm) were selected. Measured and calculated dose are

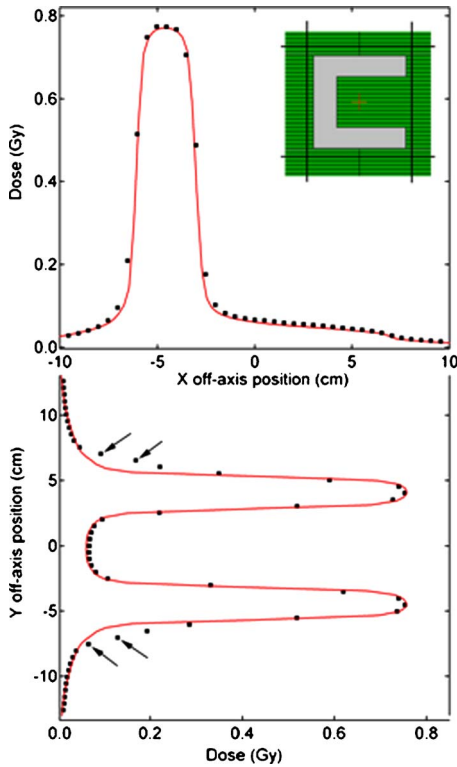


FIG. 10. Measured (IC) and calculated (AAA 7.5.18.8) orthogonal beam profiles through the central axis of a C-shaped MLC delivery (cf. inset). (100 MU, SPD=95 cm, depth=5 cm, 6 MV).

within the acceptance criteria inside the modulated area of the treatment field. The data points out of tolerance are in the low dose area, where the acceptance criterion of 2% of the local dose is difficult to achieve.

E. Inhomogeneities

1. Profiles

Figure 13 shows, for 6 MV, the calculated (SPB and AAA) and the film profiles obtained in solid water and cork

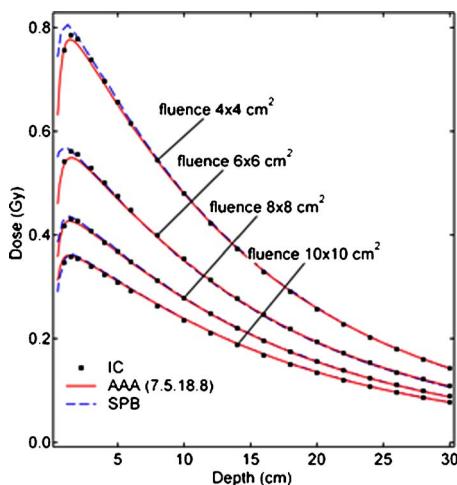


FIG. 11. Measured (IC) and calculated (SPB, AAA 7.5.18.8) depth dose curves obtained for a sweeping gap 1 cm wide, generating square fluence patterns of 10×10 , 8×8 , 6×6 , and 4×4 cm² in a fixed collimator opening of 10×10 cm². All data were obtained for 200 MU (SPD=90 cm, 6 MV).

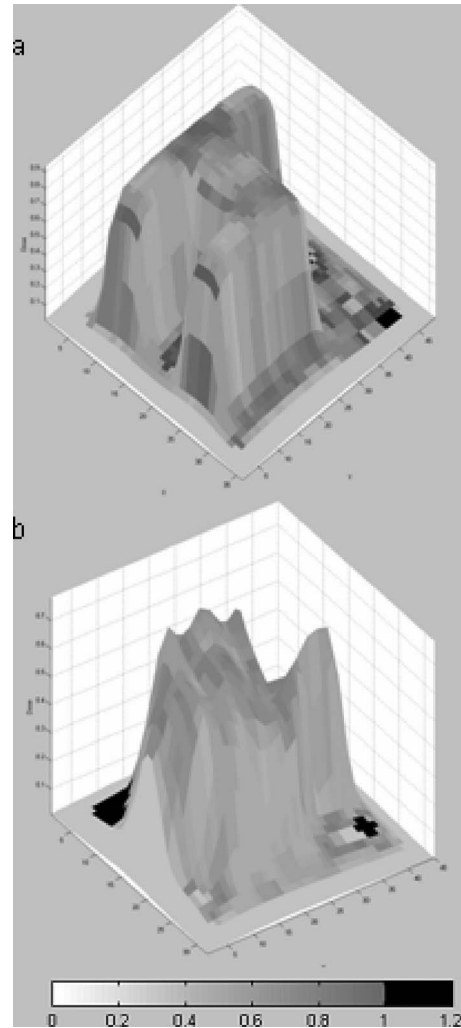


FIG. 12. Gamma evaluation comparing measured and calculated 2D dose planes (SPD=90 cm, $d=10$ cm, 6 MV) points having a gamma value larger than 1 are displayed in black, points within the acceptance criteria are displayed in shades of gray. (a) Gamma evaluation (acceptance criteria 2%, 2 mm) of the dynamic chair (depth=10 cm). (b) Gamma evaluation (acceptance criteria 3%, 3 mm) of a clinical IMRT field for a head and neck treatment.

for three field sizes (6×6 , 10×10 , and 20×20 cm²) at the depth d_2 [cf. Fig. 2(a)]. Figure 14 shows similar data for 18 MV. For the 6×6 cm² field, including only 1 cm of cork, the typical oscillating dose pattern at the interface is not visible, neither with SPB nor with AAA, but the latter offers a better agreement. AAA shows good overall correspondence for the 10×10 cm² (6 and 18 MV) and the 20×20 cm² (18 MV) field sizes, apart from an overly smoothed transition at the interface. At larger field sizes (20×20 cm²), for 6 MV, both calculation models overestimate the dose to the cork but AAA scores prominently better within the solid water. AAA considerably improves the modeling of the penumbra at the field edge in cork.

Figure 15 shows, for 6 MV, the profiles at d_1 (film and 2D ion chamber array measurements), at d_2 (film measurement), and at d_3 (film measurement) for a 15×15 cm² field size. The increasing impact of the cork on the absolute dose

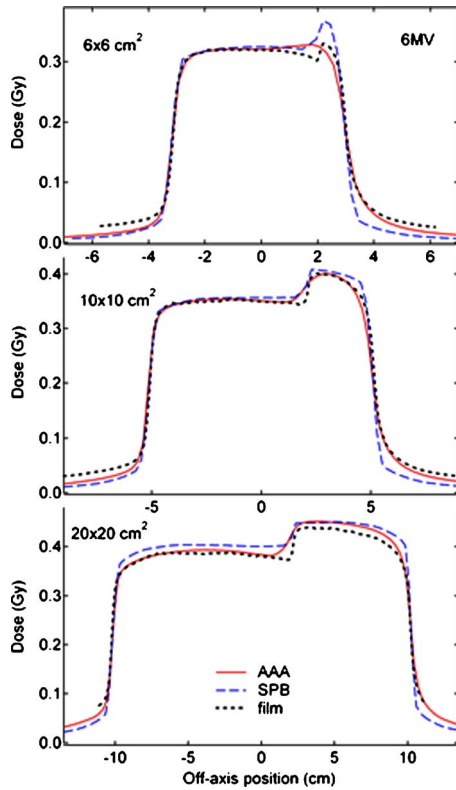


FIG. 13. Calculated and measured (film) profiles obtained in solid water and cork for three field sizes (6×6 , 10×10 , and 20×20 cm²) at the depth d2 [cf. Fig. 1(a)] for 6 MV (SPD=90 cm, 50 MU).

as a function of depth is modeled by AAA. Figure 15 also illustrates the combined use of two measurement methodologies: film and 2D ion chamber array. The array data are used to validate the film measurements in terms of absolute dose level while the film increases the profile precision. Because of its 5 mm inherent water equivalent build-up, the 2D ion chamber array cannot be used for the measurements within the cork.

Profiles at 5 mm behind the 5-cm-thick cork inhomogeneity [Fig. 2(b)] are displayed in Fig. 16 for 6 MV for field sizes 6×6 , 8×8 , and 20×20 cm². As the interface phenomena disappear, profiles are significantly better modeled.

2. Depth dose curves

Figure 17 demonstrate the depth dose behavior through solid water and cork [Fig. 2(c)] for 6 MV for field sizes 3×3 , 5×5 , 7×7 , and 15×15 cm². For the smallest field size, AAA underestimates the dose in the cork as much as the SPB overestimates it. For field sizes from 5×5 to 20×20 cm², although improvement in the calculation of the dose in the cork is achieved with AAA, SPB still models the dose behind the cork better. Below the 15-cm-thick cork inhomogeneity, AAA underestimates the dose up to 7% in the first centimeters of solid water material for the largest field size. While Fig. 18 displays similar data for 18 MV, the above-described discrepancies for 6 MV are not observed for 18 MV. While the SPB systematically overestimates the dose to the cork, especially for the smaller field sizes, sig-

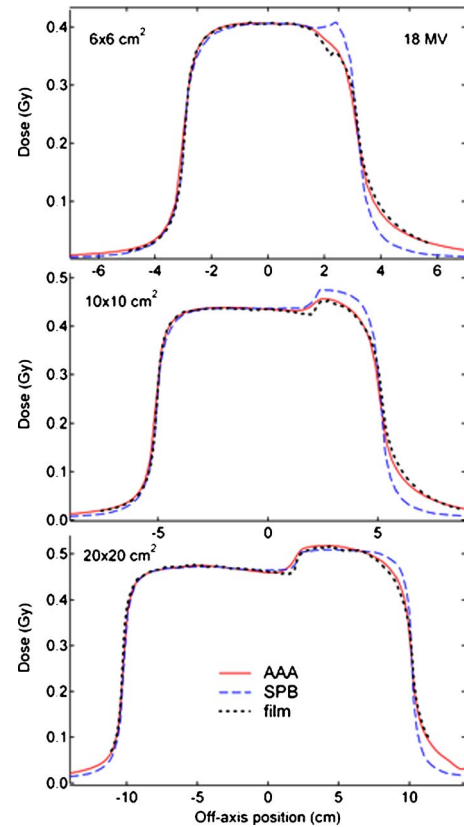


FIG. 14. Calculated and measured (film) profiles obtained in solid water and cork for three field sizes (6×6 , 10×10 , and 20×20 cm²) at the depth d2 [cf. Fig. 1(a)] for 18 MV (SPD=90 cm, 50 MU).

nificant improvement is achieved with the AAA calculation. In contrast to the 6 MV results, the dose behind the cork is also modeled within an accuracy of 2.5% (except for the 3×3 cm² field size).

3. Anthropomorphic measurements

The results for the point dose measurements in the anthropomorphic phantom are given in Table IV. When prescribing the dose to the mediastinum, for a right lateral treatment beam, AAA will overestimate the dose to the isocenter by 2% to 6% for 6 MV and by 1% to 4% for 15 MV. For 6 MV, the dose discrepancy in the isocenter increases with increasing field size, while the dose to the right lung is underestimated for the smallest field sizes. This is in agreement with the observations in the depth dose behavior in cork. In general, Table IV provides an overview of the accuracies that can be obtained in clinical situations.

4. Inhomogeneity correction and IMRT

The results of the tests performed on the heterogeneity correction during inverse planning are not shown. They are consistent with the data shown in Figs. 13–16. The inverse planning modifies the optimal fluence to compensate for the dose difference in cork according to the modified Bath³¹ heterogeneity correction, i.e., according to the SPB results shown in Figs. 13–16. SPB forward calculation reports a

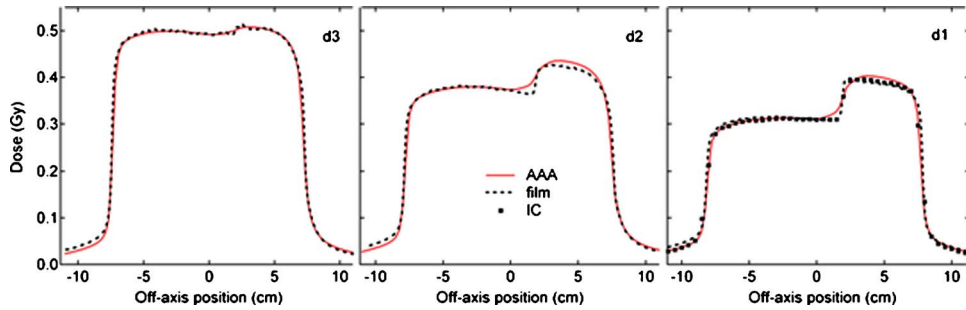


FIG. 15. Calculated (AAA) profiles for 6 MV at d1 (film and array measurements), at d2 (film measurement), and at d3 (film measurement) for a 15 × 15 cm² field size [cf. Fig. 1(a)] (SPD=90 cm, 50 MU).

homogeneous dose distribution throughout the PTV whereas measurement and AAA show overcompensation and thus an underdosage of the cork part of the PTV.

V. DISCUSSION

A. Open and wedged fields

Comparison between measured and calculated basic beam data shows that the optimization algorithm of the configuration module successfully models the parameters and correction curves required by the multiple source model. Some of the beam data used in the testing even had some measurement artifacts: one case had missing side scatter in the large-field half-profiles and another case had a slight offset in the central axis position. All artifacts were intercepted and automatically corrected for prior to optimization. For all centers, basic beam data for open fields and fields containing physical wedges are reproduced with an accuracy of 1%, 1 mm below d_{max} and 3%, 1 mm in the build-up region. Monitor units for

the symmetric fields in reference conditions are reproduced with an accuracy of 0.2%. These findings are in agreement with the results reported by Fogliata *et al.*²⁴ Because of the deviations in the modeling of the build-up area, it is not recommended to configure AAA using reference data at the depth of maximum dose. Centers having output factor tables defined at d_{max} should remeasure the output factors at a greater depth (e.g., SPD=90 cm, $d=10$ cm).

Since the beam configuration optimization algorithm is designed to yield parameters that reproduce the basic beam data, the aforementioned results are not sufficient for the acceptance of the AAA dose calculation algorithm. While the

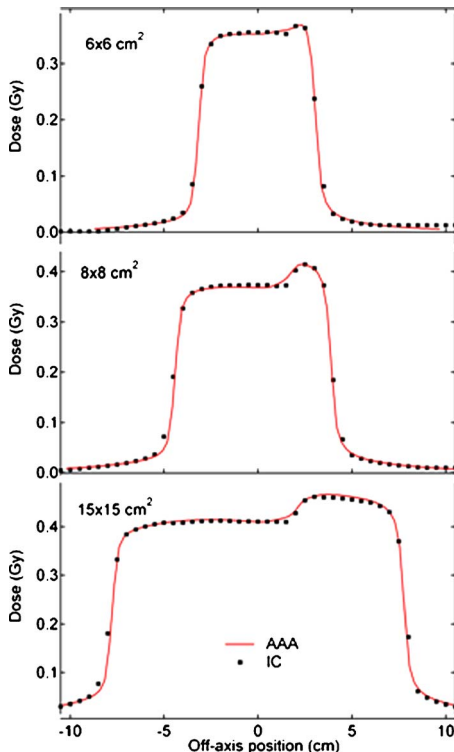


FIG. 16. Calculated and measured (IC) profiles at p1 for 6 MV for field sizes 6 × 6, 8 × 8, and 20 × 20 cm² [cf. Fig. 1(b)] (SPD=90 cm, 50 MU).

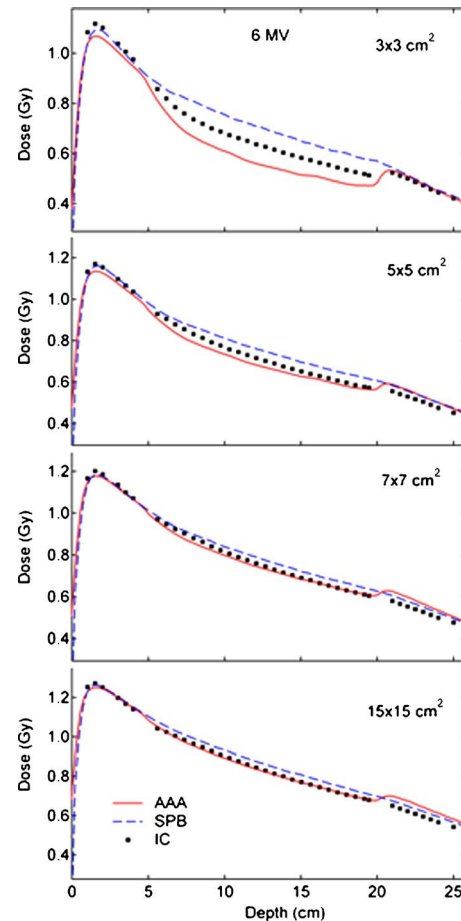


FIG. 17. Calculated (AAA and SPB) and measured depth dose curves through cork [cf. Fig. 1(c)] for 6 MV for field sizes 3 × 3, 5 × 5, 7 × 7, and 15 × 15 cm² (SPD=90 cm, 100 MU).

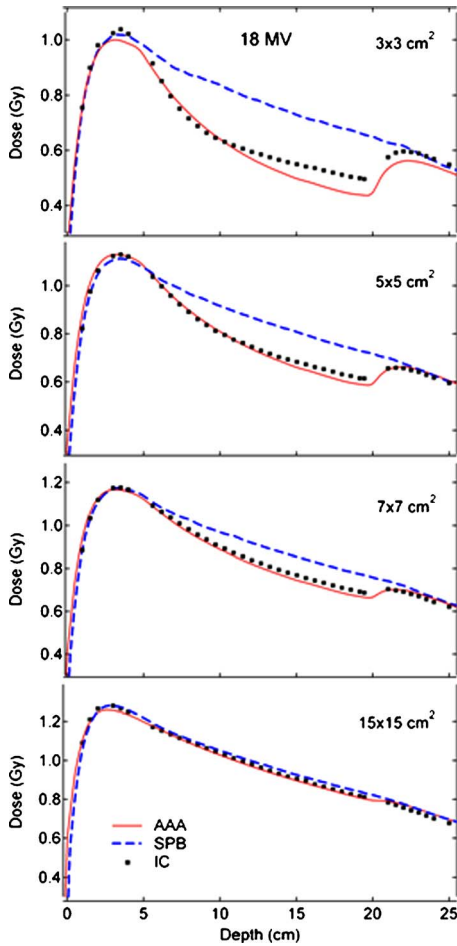


FIG. 18. Calculated (AAA and SPB) depth dose curves and measured depth dose curves in cork [phantom of Fig. 1(c)] for 18 MV for field sizes 3×3 , 5×5 , 7×7 , and 15×15 cm² (SPD=90 cm, 100 MU).

beam configuration was performed for SPD=100 cm, most tests of the dose calculation were performed at the more clinically relevant SPD=90 cm. The profile calculations for symmetric open and wedged (physical or enhanced dynamic wedges) fields show good agreement with the measurements. The introduction of the finite-size second source represents a considerable improvement in the modeling of the penumbra compared to the SPB. For AAA, the DTA is mostly within

TABLE IV. Absolute dose accuracy for point dose measurements (left and right lungs, mediastinum) in the thorax phantom (Fig. 2) for 6 and 15 MV, for different field sizes. Listed values are the ratio of calculated over measured data.

| $\Delta(\text{AAA}/\text{IC})$ (%) | | Right lung | Isocenter | Left lung |
|------------------------------------|--------------------------------|------------|-----------|-----------|
| 6 MV | 3×3 cm ² | -4.2 | 2.3 | -5.5 |
| | 5×5 cm ² | -1.2 | 3.7 | -4.8 |
| | 10×10 cm ² | 1.6 | 4.7 | -5.2 |
| | 15×15 cm ² | 2.6 | 5.3 | -3.6 |
| 15 MV | 3×3 cm ² | 5.3 | 1.8 | 5.9 |
| | 5×5 cm ² | 4.4 | 3.0 | 0.1 |
| | 10×10 cm ² | 2.0 | 3.4 | -1.6 |
| | 15×15 cm ² | 2.9 | 3.4 | 0.6 |

1 mm. The open-field depth dose curves are also well modeled for different SPD, except for the deviations in the build-up area, caused by the oversimplified modeling of the electron contamination. The limitations of the electron contamination model are particularly prominent for the physical wedge: although the depth dose calculation agrees well (1%, 1 mm) with the beam configuration data for the largest field size (15×15 cm²), measurements performed at different SPD revealed the inadequate modeling of the build-up area as a function of distance to the source, in particular for 18 MV. Evaluation of the algorithm for open and wedged fields in asymmetric geometries showed some deterioration with respect to the symmetric beam data: deviations up to 3% of the absolute dose at the center of the field were observed for the most extreme setups. These deviations are suspected to be related to inaccuracies in the MU calculation—more specifically in the calculation of the HSF or CBSF—for highly asymmetric collimator settings.

The results obtained on the accuracy of the wedge are comparable to the ones reported for other planning systems. For the collapsed cone convolution superposition algorithm, implemented in the Pinnacle TPS, Lydon⁸ reported an accuracy for the modeling of open and wedged beams (symmetric and asymmetric collimator settings) of 2% or 2 mm. Liu *et al.*^{6,7} investigated—also for the Pinnacle system—the accuracy of hard wedges and dynamic wedges and reported an accuracy of 2% and 0.5%, respectively. Similar results were reported by Bedford *et al.*⁵

B. Static and dynamic MLC shaped fields

Some geometrically simple tests showed an error in the absolute dose calculation for static (and dynamic) MLC fields. When calculating the head scatter factor, only the MLC and not the main collimator was taken into account. A corrected β -version (7.5.18.8) was supplied for further testing. In contrast to the wedged fields, the electron contamination model appears adequate for MLC fields. The MLC tests also highlight the fact that the MLC's rounded leaf ends are not taken into account in the fluence calculation for a static MLC. This is not of major importance in most conventional MLC fields because closed leaf pairs are usually positioned with their touching leaf tips under the main collimators. Leakage through the closed leaf tips as well as changes of the effective MLC opening could become an issue when multiple consecutive small static MLC segments are used to mimic an IMRT treatment without using the Eclipse leaf motion calculator. As the dosimetric leaf separation is a parameter already available in the planning system for fluence calculation of dynamic MLC fields, applying this parameter to the static MLC fields would be a straightforward improvement.

Since the Eclipse inverse planning module as well as the leaf motion calculator are unaffected by the AAA forward dose calculation, IMRT tests were limited to a few critical cases. Although the initial tests with version 7.5.14.3 showed the same discrepancies as noticed for the static MLC fields, with version 7.5.18.8 overall agreement between the depth

dose curves for the narrow sweeping gap is better than 1%, 1 mm, provided adequate MLC parameters are supplied by the user. Although deviations of up to 3% are again observed around d_{\max} , modeling of dose in the build-up area is better for AAA than for SPB, especially for fields targeting only a small fraction of the field opening defined by the main collimators. Measurements of the dynamic chair, often used in the process of IMRT commissioning, show 2%, 2 mm agreement with the AAA dose calculation, comparable to what can be obtained with SPB (provided the SPB kernels have been carefully validated for IMRT purposes). Verification of clinical IMRT fields in a homogeneous phantom also show results comparable to the ones obtained with SPB. A typical illustration is given in Fig. 12(b). It may be worthwhile to mention that, since no modifications have been done to the leaf motion calculator, the generation of the actual fluence remains the same as in previous versions, implying that the tongue and groove effect remains unaccounted for in the dose calculation.³²

C. Inhomogeneities

The most important approximation in the photon (primary and secondary) dose calculation relates to the fact that the dose calculation is split up into a depth-dependent and a lateral scatter component, describing the photon interactions through attenuation along the incident beamlet direction and subsequent scatter in a plane perpendicular to it. This is clearly an approximation that will affect accuracy of the heterogeneity correction since it does not take the divergent scatter of heterogeneities from upper levels correctly into account. Another approximation comes from the fact that a discrete number of angular sectors has to be used. This will mostly cause smoothening out of the calculated dose distribution near heterogeneous interfaces. These approximations are reflected in the comparison of the measured and calculated data in heterogeneous media.

Profiles through solid water and cork show the improved modeling of the penumbra at the field edge in cork. Even though the dose calculation at the interface is still suboptimal, AAA offers a better agreement than SPB, especially when only limited amounts of cork are included in the irradiated field. AAA calculations display the fast drop in the dose at the water/cork interface for 18 MV. This agrees well with the findings of other authors having investigated the energy choice of treatment for lung cancers. Using SPB algorithms, the target coverage with 18 MV is significantly underestimated when using small margins. Hence it has been stated that 6 MV is the energy of choice for the irradiation of lung tumors.³³ The behavior of this interface dose was also investigated by Martens *et al.*³⁴ and by Arnfield *et al.*⁹ for the collapsed cone convolution algorithm implemented in the Helax and in the Pinnacle treatment planning system. Both groups concluded that the collapsed cone convolution algorithms were not able to calculate the interface dose very accurately, but provided a considerable improvement to pencil beam algorithms.

For 6-MV photon beams, the dose calculation as a function of depth in a slab phantom is not significantly better modeled with AAA than with SPB. Although the dose within the cork is more accurately reported on for field sizes larger than 7×7 cm², the dose in the first centimeters behind the 15-cm-thick cork slab is overestimated by up to 7%, whereas SPB overestimates only by 3% to 4% in that area. For 18 MV, AAA shows unmistakable improvement in the depth dose calculation in cork when compared to SPB since the latter systematically overestimates the dose in lung. This better modeling of the dose in the lung was also reported by Nisbet *et al.*³⁵ and by Aspradakis *et al.*¹¹ for the collapsed cone convolution model implemented in Helax (Nucletron, the Netherlands) and Pinnacle (Philips, UK). The systematic overestimation of the dose in lung when using commercial pencil beam systems was also reported by different groups.^{11,13,17} In contrast to 6 MV, for 18 MV, the AAA overestimation of the dose behind the cork is not observed. The fact that AAA performs better for 18 MV than for 6 MV is related to the above mentioned approximation. Low-energy photons produce a larger amount of divergent scatter, whereas the more forward directed scattering of the high-energy photons is better approached by the assumed pathways.

The change in the estimated dose in the lung is likely to affect clinical practice considerably: as the dose volume histograms of the lungs will substantially decrease with AAA, so will the parameters such as V20 or V25 used by clinicians to decide upon the adequacy of a plan. When switching from SPB to AAA, clinicians should be aware of the risk of unknowingly increasing the true accepted dose to lung.

Although the anthropomorphic phantom provides a more clinical verification of the accuracy that can be obtained with AAA, its more complex geometry makes the interpretation of the results less obvious. In general, findings are in agreement with the AAA behavior observed in the slab geometries. As a general guideline, for a lateral treatment beam, the dose to the lung as well as to the mediastinum will typically be within 5% (under- or overdosage) of the calculated value.

Making use of the modified Batho heterogeneity correction, the inverse planning algorithm does not always adequately take heterogeneities into account. Whereas the final forward dose calculation with SPB (and the modified Batho law) falsely reports a successful homogeneous dose delivery to the inhomogeneous target volume, AAA however, at least reports on the obtained dose more accurately. If the user so desires, manual modifications to the optimal fluence can be performed in the fluence editor of the planning system to obtain better inhomogeneity compensation and more homogeneous target coverage, but this is an intuitive and iterative task.

Although some of the simplifications and approximations made in the algorithm have their impact on the robustness of dose modeling in a variety of setups, they have the advantage of speeding up the dose calculation considerably. Calculation times for AAA are comparable to those for SPB.

VI. CONCLUSION

The implementation of AAA represents an improvement for the Eclipse TPS at the level of dose accuracy, i.e., compared to the single pencil beam model. Improvements concern the modeling of the penumbra and the low dose regions, as well as the field profiles for (symmetric and asymmetric) open and wedged fields. The electron contamination model, however, fails to report accurately on the dose in the build-up area. Dose calculations to heterogeneous media show considerable improvement, especially for the high-energy photon beams, but suboptimal modeling of the dose at the interface is still observed.

ACKNOWLEDGMENTS

The authors acknowledge Martin Morelle and Sebastien Bontemps (Department of Radiotherapy, Namur, Belgium) and Elisabetta Cagni (Department of Medical Physics, Reggio Emilia, Italy) for providing assistance in the measurements. This work was supported by a grant of Varian Medical Systems. The authors wish to thank PTW (Freiburg, Germany) for providing the Seven29 2D ion chamber array. They also wish to thank Joakim Pyyry and Katja Pesola for the many fruitful discussions regarding the algorithm and Janne Sievinen for his kind help in the collaboration with the different centers.

^{a)} Author to whom correspondence should be addressed; electronic mail: ann.vanesch@7sigma.be

- ¹D. Low and S. Mutic, "A commercial IMRT treatment-planning dose-calculation algorithm," *Int. J. Radiat. Oncol., Biol., Phys.* **41**, 933–937 (1998).
- ²C. T. Baird, G. Starkschall, H. H. Liu, T. A. Buchholz, and K. R. Hogstrom, "Verification of tangential breast treatment dose calculations in a commercial 3D treatment planning system," *J. Appl. Clin. Med. Phys.* **2**, 73–84 (2001).
- ³H. Hansson, P. Bjork, T. Knoos, and P. Nilson, "Verification of a pencil based treatment planning system: output factors for open photon beams shaped with MLC or blocks," *Phys. Med. Biol.* **44**, 201–207 (1999).
- ⁴K. A. Gifford, D. Followill, H. H. Liu, and G. Starkschall, "Verification of the accuracy of a photon dose-calculation algorithm," *J. Appl. Clin. Med. Phys.* **3**, 26–45 (2002).
- ⁵J. L. Bedford, P. J. Childs, V. Nordmark Hansen, M. A. Mosleh-Shirazi, F. Verhaegen, and A. P. Warrington, "Commissioning and quality assurance of the Pinnacle(3) radiotherapy treatment planning system for external beam photons," *Br. J. Radiol.* **76**, 163–176 (2003).
- ⁶H. H. Liu, T. R. Mackie, and E. C. McCullough, "Calculating dose and output factors for wedged photon radiotherapy fields using a convolution/superposition method," *Med. Phys.* **24**, 1714–1728 (1997).
- ⁷H. H. Liu, E. C. McCullough, and T. R. Mackie, "Calculating dose distributions and wedge factors for photon treatment fields with dynamic wedges based on a convolution/superposition method," *Med. Phys.* **25**, 56–63 (1998).
- ⁸J. M. Lydon, "Photon dose calculations in homogeneous media for a treatment planning system using a collapsed cone superposition convolution algorithm," *Phys. Med. Biol.* **43**, 1813–1822 (1998).
- ⁹M. R. Arnfield, C. H. Siantar, J. Siebers, P. Garmon, L. Cox, and R. Mohan, "The impact of electron transport on the accuracy of computed dose," *Med. Phys.* **27**, 1266–1274 (2000).
- ¹⁰M. Miften, M. Wiesmeyer, S. Monhofer, and K. Krippner, "Implementation of FFT convolution and multigrid superposition models in the FOCUS RTP system," *Phys. Med. Biol.* **45**, 817–833 (2000).

- ¹¹M. M. Aspradakis, R. Morrison, N. Richmond, and A. Steele, "Experimental verification of convolution/superposition photon dose calculations for radiotherapy treatment planning," *Phys. Med. Biol.* **48**, 2873–2893 (2003).
- ¹²V. Borca Casanova, M. Pasquino, S. Bresciani, P. Catuzzo, F. Ozello, and S. Tofani, "American Association of Physicists in Medicine, Dosimetric evaluation of a commercial treatment planning system using the AAPM Task Group 23 test package," *Med. Phys.* **32**, 744–751 (2005).
- ¹³P. N. McDermott, T. He, and A. DeYoung, "Dose calculation accuracy of lung planning with a commercial IMRT treatment planning system," *J. Appl. Clin. Med. Phys.* **4**, 341–351 (2003).
- ¹⁴I. J. Chetty, P. M. Charland, N. Tyagi, D. L. McShan, B. A. Fraass, and A. F. Bielajew, "Photon beam relative dose validation of the DPM Monte Carlo code in lung-equivalent media," *Med. Phys.* **30**, 563–573 (2003).
- ¹⁵I. J. Chetty, M. Rosu, D. L. McShan, B. A. Fraass, and R. K. Ten Haken, "The influence of beam model differences in the comparison of dose calculation algorithms for lung cancer treatment planning," *Phys. Med. Biol.* **50**, 801–815 (2005).
- ¹⁶M. F. Tsiakalos, K. Theodorou, C. Kappas, S. Zefkili, and J. C. Rosenwald, "Analysis of the penumbra enlargement in lung versus the quality index of photon beams: a methodology to check the dose calculation algorithm," *Med. Phys.* **31**, 943–949 (2004).
- ¹⁷W. Ding, P. N. Johnston, and I. F. Bubb, "Investigation of photon beam models in heterogeneous media of modern radiotherapy," *Australas. Phys. Eng. Sci. Med.* **27**, 39–48 (2004).
- ¹⁸A. Ahnesjö, "Collapsed cone convolution of radiant energy for photon dose calculation in heterogeneous media," *Med. Phys.* **16**, 577–592 (1989).
- ¹⁹W. Ulmer and D. Harder, "A triple Gaussian pencil beam model for photon beam treatment planning," *Z. Med. Phys.* **5**, 25–30 (1995).
- ²⁰W. Ulmer and D. Harder, "Applications of a triple Gaussian pencil beam model for photon beam treatment planning," *Z. Med. Phys.* **6**, 68–74 (1996).
- ²¹J. Sievinen, W. Ulmer, and W. Kaissl, "AAA photon dose calculation in Eclipse," Varian documentation RAD #7170B, 2005.
- ²²W. Ulmer, J. Pyyry, and W. Kaissl, "A 3D photon superposition/convolution algorithm and its foundation on results of Monte Carlo calculations," *Phys. Med. Biol.* **50**, 1767–1790 (2005).
- ²³P. Storchl and E. Woudstra, "Calculation of the absorbed dose distribution due to irregularly shaped photon beams using pencil beam kernels derived from basic beam data," *Phys. Med. Biol.* **41**, 637–656 (1996).
- ²⁴A. Fogliata, G. Nicolini, E. Vanetti, A. Clivio, and L. Cozzi, "Dosimetric validation of the anisotropic analytical algorithm for photon dose calculation: fundamental characterization in water," *Phys. Med. Biol.* **51**, 1421–1438 (2006).
- ²⁵H. Liu, T. Mackie, and E. McCullough, "A dual source photon beam model used in convolution/superposition dose calculations for clinical megavoltage x-rays beams," *Med. Phys.* **24**, 1960–1974 (1997).
- ²⁶I. Kawrakow and D. Rogers, "The EGSnrc code system: Monte-Carlo simulation of electron and photon transport," NRCC Report PIRS-701, 2003.
- ²⁷I. Kawrakow, "Accurate condensed history Monte Carlo simulations of electron transport. I. EGSnrc, the new EGS4 version," *Med. Phys.* **27**, 485–498 (2000).
- ²⁸A. Van Esch, J. Bohsung, P. Sorvari, M. Tenhunen, M. Paiusco, M. Iori, P. Engström, H. Nyström, and D. P. Huyskens, "Acceptance tests and quality control (QC) procedures for the clinical implementation of IMRT using inverse planning and the sliding window technique: experience from five radiotherapy departments," *Radiother. Oncol.* **65**, 53–70 (2002).
- ²⁹D. A. Low, W. B. Harms, M. Sasa, and J. A. Purdy, "A technique for the quantitative evaluation of dose distributions," *Med. Phys.* **25**, 656–661 (1998).
- ³⁰T. Depuydt, A. Van Esch, and D. P. Huyskens, "A quantitative evaluation of IMRT distributions: refinement and clinical assessment of the gamma evaluation," *Radiother. Oncol.* **62**, 309–319 (2002).
- ³¹H. F. Batho, "Lung corrections in Cobalt 60 beam therapy," *J. Can. Assoc. Radiol.* **15**, 39–83 (1964).
- ³²M. Essers, M. de Langen, M. L. P. Dirks, and B. J. M. Heymen, "Commissioning of a commercially available system for intensity-modulated radiotherapy dose delivery with dynamic multileaf collimation," *Radiother. Oncol.* **60**, 215–244 (2001).
- ³³R. C. Miller, J. A. Bonner, and R. Kline, "Impact of beam energy and field margin on penumbra at lung tumor-lung parenchyma interfaces," *Int.*

- J. Radiat. Oncol., Biol., Phys. **41**(3), 707–713 (1998).
- ³⁴C. Martens, N. Reynaert, C. De Wagter, P. Nilsson, M. Coghe, H. Palmans, H. Thierens, and W. De Neve, “Underdosage of the upper-airway mucosa for small fields as used in intensity-modulated radiation therapy: a comparison between radiochromic film measurements, Monte Carlo simulations, and collapsed cone convolution calculations,” *Med. Phys.* **29**, 1528–1535 (2002).
- ³⁵A. Nisbet, I. Beange, H. Vollmar, C. Irvine, A. Morgan, and D. Thwaites, “Dosimetric verification of a commercial collapsed cone algorithm in simulated clinical situations,” *Radiother. Oncol.* **73**, 79–88 (2004).